Voltage-activated parametric entangling gates based on gatemon qubits

Yinqi Chen[®], ^{1,*} Konstantin N. Nesterov[®], ^{1,2} Hugh Churchill, ³ Javad Shabani, ⁴ Vladimir E. Manucharyan, ^{5,6} and Maxim G. Vavilov¹

Department of Physics and Wisconsin Quantum Institute, University of Wisconsin-Madison, Madison, Wisconsin 53706, USA

²Bleximo Corp., Berkeley, California 94710, USA

Department of Physics, University of Arkansas, Fayetteville, Arkansas 72701, USA

Center for Quantum Information Physics, Department of Physics, New York University, New York 10003, USA
Department of Physics, Joint Quantum Institute, and Quantum Materials Center, University of Maryland,
College Park, Maryland 20742, USA

⁶EPFL, CH-1015 Lausanne, Switzerland



(Received 25 April 2023; revised 25 August 2023; accepted 6 September 2023; published 5 October 2023)

We describe the generation of entangling gates on superconductor-semiconductor hybrid qubits by ac voltage modulation of the Josephson energy. Our numerical simulations demonstrate that the unitary error can be below 10^{-5} in a variety of 75-ns-long two-qubit gates (CZ, iSWAP, and \sqrt{i} SWAP) implemented using parametric resonance. We analyze the conditional ZZ phase and demonstrate that the CZ gate needs no further phase-correction steps, while the ZZ phase error in SWAP-type gates can be compensated by choosing pulse parameters. With decoherence considered, we estimate that qubit relaxation time needs to exceed 70 μ s to achieve the 99.9% fidelity threshold.

DOI: 10.1103/PhysRevApplied.20.044012

I. INTRODUCTION

Two-qubit gates present a challenge in the development of scalable superconducting quantum processors. In the simplest hardware architectures based on fixed-frequency qubits and always-on couplings, two-qubit gates can be realized by microwave control [1–4] via, for example, the cross-resonance effect [5–7]. Nevertheless, gates with fixed-frequency transmon qubits [8] and fixed couplings lead to stringent frequency allocation conditions [9], which complicate processor design and reduce the yield of multiqubit chips in microfabrication. An alternative way is to make qubit frequencies tunable so that two-qubit states can be moved into and out of resonance conditions to induce transitions between qubit states or to enable conditional phase accumulations [10–14].

While the tunability adds more freedom for gate and processor design, it may reduce the processor's performance due to the crowded spectrum of multiqubit systems [15]. During the frequency-tuning process, one can cross unintended resonances, making it hard to control specific pairs of qubits without inducing spectator errors in other qubits. One approach to avoid crossing undesirable resonances is to induce a parametric resonance on a desired pair of qubits. The latter can be achieved by modulating

qubit frequencies [16–23] or coupling elements [24–30]. The parametric resonance response is determined by the modulation amplitudes and frequencies, thus one can target a specific pair in an array of qubits with similar frequencies. For flux-tunable transmon qubits, frequency modulation has been realized by varying the external flux bias through the superconducting quantum interference device (SQUID) loop, which changes the effective Josephson energy [19,20,30]. The SQUID loop makes qubits susceptible to flux noise and limits their coherence time. Maintaining long coherence of flux-tunable qubits remain a challenging task [31].

Another way to control the qubit characteristics is to use voltage-tunable qubits, so-called "gatemons," where the metallic gate voltage controls the charge-carrier density in the Josephson junctions [32–35]. The gate voltage control eliminates flux noise sensitivity [34] and suppresses charge dispersion [36]. Furthermore, voltage control is a well-developed technology for classical electronics and can be readily applied to the gatemon qubits. Despite these advantages, the voltage control method introduces charge noise to the qubit. While the suppression of charge noise on gatemon qubits has been improved in recent years, gatemons at current stage still have relatively low coherence time, which limits the achievable fidelity of gate operations. For the successful realization of two-qubit gates, a certain threshold on coherence has to be met.

^{*}chen447@wisc.edu

In this paper, we analyze the possibility of implementing entangling gates on gatemon qubits by voltage modulation of the Josephson energy and estimate the requirements for gatemon coherence. We look at three types of entangling gates that belong to different classes of local equivalence: (i) the CZ gate, (ii) the *i*SWAP gate, and (iii) the \sqrt{i} SWAP gate. We computationally show that all three gates can be implemented with fidelity >99.99% for unitary evolution. Once decoherence is taken into consideration, the fidelity greater than 99.9% requires that the relaxation time T_1 exceeds 70 μ s.

We analyze the error budget and identify several primary coherent-error mechanisms for the two-qubit gates. In particular, we find that the unwanted conditional ZZ phase is the most harmful error for SWAP-type gates and propose mitigation of this error using qubit tunability. Because of its simplicity, this mitigation approach is beneficial in comparison to resorting to advanced pulse-shape designs [37] or to tunable couplers [38,39], which add complexity to the control scheme. For the iSWAP gate, we demonstrate that the accumulated ZZ phase can be reduced to zero by tuning the static Josephson energy for an experimentally accessible range of the coupling constant. For \sqrt{i} SWAP, the parameter range of suppressed phase error is wider and can be further expanded by using a two-tone modulation pulse with close frequencies.

The paper is organized as follows. In Sec. II, we introduce the Hamiltonian of interacting gatemon qubits that we use to model entangling gates. In Sec. III we present the simulation of the CZ gate, showing that the CZ gate can be optimized to high fidelity >99.99% for a broad range of coupling constant J_C . In Sec. IV, we present the simulation of the iSWAP gate, analyze the detrimental effect of ZZ phase on the gate fidelity, and discuss how this phase can be compensated by choosing appropriate static Josephson energy. In Sec. V, we present the simulation of the \sqrt{i} SWAP gate and similarly discuss how the ZZ phase can be compensated. We do this for both one-tone and twotone pulse schemes. In Sec. VI, we evaluate the effect of decoherence on gate fidelity and discuss requirements on the relaxation time T_1 of future-generation gatemon qubits to enable high-fidelity gates.

II. BASIC MODEL

A. Qubit Hamiltonian

The idea of implementing two-qubit gates by directly modulating qubit spectra has been proposed and realized on transmon qubits [19–23]. With the proper choice of frequencies, modulation pulses can selectively induce Rabi oscillations between desired states to generate gates. For transmons, the qubit-frequency modulation is achieved by tuning the external magnetic field. Here we apply the idea of parametric control onto gatemon qubits using gate

voltage as the control instead of the external magnetic field.

In a gatemon qubit, the Josephson junction (JJ) is implemented with a superconductor—normal-metal—superconductor (S-N-S) structure, where the normal section is a semiconductor. The semiconductor allows Josephson energy E_J to be tuned by the gate voltage V_g [32,33,35,40]. The quantum system then consists of a fixed qubit (F) and a gate-tunable qubit (T) with capacitive coupling, as shown in Fig. 1. The Hamiltonian of this circuit is

$$\hat{H} = \hat{H}_F + \hat{H}_T + J_C \hat{n}_F \hat{n}_T, \tag{1}$$

where \hat{H}_i (i = F, T) are single-qubit Hamiltonians

$$\hat{H}_{l} = 4E_{C,l}\hat{n}_{l}^{2} - E_{J,l}\cos(\hat{\varphi}_{l}), \qquad (2)$$

and $\hat{n}_t, \hat{\varphi}_t$ are the charge and phase operators. The charge coupling constant J_C is determined by the capacitances of circuit components [41]. The parameters $E_{C,t}$ and $E_{J,t}$ are, respectively, the charging and Josephson energies, which obey the standard transmon condition $E_{J,t} \gg E_{C,t}$ [8]. For the gatemon qubit considered here, $E_{J,T}$ is not controlled by flux bias, but instead by the gate voltage V_g :

$$E_{J,T} = E_{J,T}(V_g)$$
. (3)

For an actual device, the dependence of E_J on V_g does not have a simple relation. However, we will assume a first-order approximation in the current theoretical study:

$$E_{J,T}(V_0 + \delta V_g) = E_{J,T}(V_0) + E'_{J,T}(V_g) \big|_{V_{\sigma} = V_0} \delta V_g.$$
(4)

A sinusoidal pulse of voltage will induce sinusoidal oscillation of $E_{J,T}$

$$E_{J,T}(t) = \bar{E}_{J,T} + f(t)\delta E_{J,T}\cos(\omega_p t), \qquad (5)$$

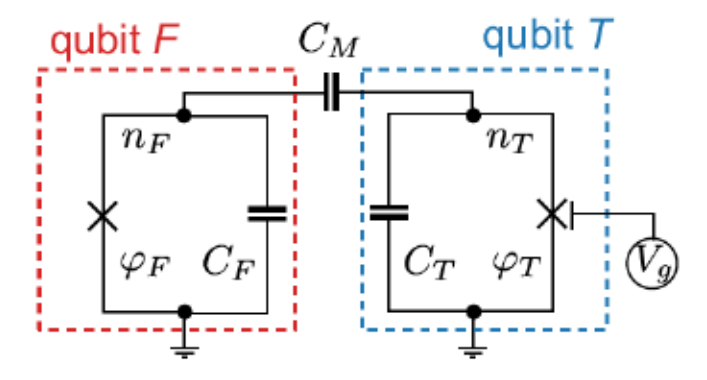


FIG. 1. Circuit diagram of two capacitively coupled gatemon qubits. The Josephson junction of the tunable qubit (T) is gated by a voltage V_g , which can be used to control the Josephson energy $E_{J,T}$ of the tunable qubit.

where ω_p is the modulation frequency, $\delta E_{J,T}$ is the amplitude of the modulation, and $E_{J,T}$ is the *static* Josephson energy. We use a Gaussian flat-top envelope f(t) defined as

$$f(t) = \begin{cases} \exp\left(-\frac{2(t - t_{\text{left}})^2}{t_{\text{rise}}^2}\right) - e^{-2} & 0 < t < t_{\text{left}} \\ 1 - e^{-2} & t_{\text{left}} < t < t_{\text{right}} \\ \exp\left(-\frac{2(t - t_{\text{right}})^2}{t_{\text{rise}}^2}\right) - e^{-2} & t_{\text{right}} < t < t_{\text{gate}}, \end{cases}$$
(6)

where $t_{\text{left}} = t_{\text{rise}}$, $t_{\text{right}} = t_{\text{gate}} - t_{\text{rise}}$. Here t_{rise} is the ramping time for the pulse to ramp up and down, and t_{gate} is the gate time.

We want to point out that for flux-tunable qubits it is common to park at sweet spots [20], which are characterized by a second-ordered dependence of E_J on the tuning parameter. Here we differ by choosing a linear dependence between E_J and V since we do not specifically assume the existence of a voltage sweet spot. If such a sweet spot exists, driving at the sweet spot is also viable and is likely beneficial. In comparison to the linear dependence on V, when the first-harmonic term of ω_p yields a qubit drive, the quadratic dependence on V results in the qubit drive being produced by the second-harmonic term.

We denote the fixed-qubit frequency by ω_F , and write the time-dependent tunable-qubit frequency ω_T in the presence of the voltage modulation, Eq. (5), as the Fourier series:

$$\omega_T(t) = \tilde{\omega}_T + \sum_{m=1}^{\infty} \delta \omega_m \cos(m\omega_p t). \tag{7}$$

We also write $\eta_F > 0$ for the absolute value of the fixedqubit anharmonicity and use $\bar{\eta}_T > 0$ for the time-averaged anharmonicity of the tunable qubit.

In numerical simulations, we use the following qubit parameters: $E_{C,F}/h = E_{C,T}/h = 0.2$ GHz, $E_{J,F}/E_{C,F} = 100$, $\bar{E}_{J,T}/E_{C,T} = 78$. We simulate all three types of entangling gates for gate time fixed at 75 ns. The corresponding qubit frequencies and anharmonicities without modulation are $\omega_F/(2\pi) = 5.449$ GHz, $\eta_F/(2\pi) = 0.219$ GHz, $\bar{\omega}_T/(2\pi) = 4.787$ GHz, $\bar{\eta}_T/(2\pi) = 0.222$ GHz. For these system parameters, the structure of the static single-qubit spectra can be inferred from Table I. The coupling J_C ranges from 10 to 30 MHz.

As preparation for later discussion, we mention that the coupling between two qubits will introduce ZZ interaction even without any driving. The static ZZ phase accumulation rate due to this interaction is $(E_{\overline{00}} + E_{\overline{11}} - E_{\overline{01}} - E_{\overline{10}})/h$, where $E_{\overline{ij}}$ are dressed eigenenergies. For example, when $J_C = 10$ MHz and $\bar{E}_{J,T}/E_{C,T} = 78$, the ZZ phase accumulation rate is 1.41 MHz.

TABLE I. Static transition frequencies of single qubits. Units are in GHz.

Transition process	Fixed qubit	Tunable qubit
0 → 1	5.449	4.787
$1 \rightarrow 2$	5.230	4.565
$2 \rightarrow 3$	4.995	4.323

B. Parametric-resonance conditions

While we use the full-circuit Hamiltonian (1) for simulations, in this section, we identify relevant terms in the interaction-picture Hamiltonian, which dominate system dynamics for specific gates [19,20]. The choice of ω_p determines the resonance condition. For *i*SWAP processes, when $\omega_p \approx \Delta$, the relevant term is

$$\hat{H}_{iSWAP} = g_{10.01}^{(1)} e^{-i(\omega_p - \Delta)t} |10\rangle \langle 01| + \text{h.c.}$$
 (8a)

For CZ processes, the relevant term is

$$\hat{H}_{CZ}^{(1)} = g_{20,11}^{(1)} e^{i(\omega_p - \Delta - \eta_F)t} |20\rangle \langle 11| + \text{h.c.}$$
 (8b)

when $\omega_p \approx \Delta + \eta_F$ or

$$\hat{H}_{CZ}^{(2)} = g_{11.02}^{(1)} e^{i(\omega_p - \Delta + \bar{\eta}_T)t} |11\rangle \langle 02| + \text{h.c.}$$
 (8c)

when $\omega_p \approx \Delta - \bar{\eta}_T$. Here $g_{ij,kl}^{(1)}$ is the renormalized interaction matrix element, $\Delta = \bar{\omega}_T - \omega_F$ is the detuning between the time average of tunable and fixed-qubit frequencies, and $|ij\rangle = |i\rangle_F \otimes |j\rangle_T$ is the two-qubit product state corresponding to qubit F being in state $|i\rangle_F$ and T being in state $|j\rangle_T$. A more detailed discussion of the Hamiltonian terms in Eqs. (8) can be found in Appendix A.

We point out here that for the experiment with transmon qubit, parametric modulation is usually operated at the sweet spot, therefore only even-*m* harmonics are present in the corresponding analogue of the Fourier series (7) [20,23]. For demonstration in this paper, on the other hand, we choose to operate at a point where the frequency linearly depends on voltage, and thus all harmonics are present in Eq. (7).

C. Two-qubit gates

The two-qubit entangling gates can be classified by their local equivalence, i.e., whether they can be transformed into each other solely using single-qubit operations. Such classes of equivalence relations can be characterized by two local invariants [42]. We analyze the two-qubit gates

in the following form [43]:

$$\hat{U}_{\text{ideal}}(\theta,\zeta) = \begin{pmatrix} e^{-i\xi/2} & 0 & 0 & 0\\ 0 & \cos\frac{\theta}{2} & -i\sin\frac{\theta}{2} & 0\\ 0 & -i\sin\frac{\theta}{2} & \cos\frac{\theta}{2} & 0\\ 0 & 0 & 0 & e^{-i\xi/2} \end{pmatrix}.$$
(9)

In particular, we look at the three cases when

$$\zeta = \pi, \quad \theta = 0,$$
 (10a)

which is locally equivalent to the CZ gate,

$$\zeta = 0, \quad \theta = \pi,$$
 (10b)

which is the iSWAP gate, and

$$\zeta = 0, \quad \theta = \pi/2, \tag{10c}$$

which is the $\sqrt{i\text{SWAP}}$ gate. By Eqs. (8), the resonance condition for Eqs. (10b) and (10c) is $\omega_p = \Delta$, while for Eq. (10a), the condition is either $\omega_p = \Delta - \bar{\eta}_T$ or $\omega_p = \Delta + \eta_F$.

We assume that we can apply virtual single-qubit Z rotations before and after the pulses so that the evolution operator in the computational subspace can be locally transformed to the form given by Eq. (9) [44]. Therefore, the evolution operator for gate-fidelity calculations has the form:

$$\hat{U} = \hat{U}_{post} \hat{U}_{pulse} \hat{U}_{pre}, \tag{11}$$

where $\hat{U}_a = \exp(i\hat{Z}_1\vartheta_{a,1}) \exp(i\hat{Z}_2\vartheta_{a,2})$ for a = pre, post are the local Z rotations, and \hat{U}_{pulse} is the evolution induced by the pulse Eq. (4) and projected into the computational subspace. The coherent gate fidelity is then calculated using the final matrix \hat{U} as [45]

$$F = \frac{\text{Tr}(\hat{U}^{\dagger}\hat{U}) + |\text{Tr}[\hat{U}_{\text{ideal}}(\theta, \zeta)^{\dagger}\hat{U}]|^2}{20}.$$
 (12)

III. THE CZ GATE

The CZ gate can be achieved by satisfying the resonance condition $\omega_p = \Delta + \eta_F$ of $\hat{H}_{\rm CZ}^{(1)}$, see Eq. (8b), or $\omega_p = \Delta - \bar{\eta}_T$ of $\hat{H}_{\rm CZ}^{(2)}$, see Eq. (8c). Here we choose the latter condition for simulation. With this choice of ω_p , a 2π rotation in the $|11\rangle - |02\rangle$ subspace transforms state $|11\rangle$ into $e^{i\pi}$ $|11\rangle$, thus inducing a CZ gate.

The evolution of the system is defined by additional terms of the full Hamiltonian that are presented in Appendix A. Although these terms result in small corrections, we take them into account in numerical simulations. Here we briefly identify these terms. (i) There is small off-resonant phase accumulation for states |00\, |01\, |10\ due to ac Stark effect, see Appendix B. (ii) The transitions $|00\rangle \leftrightarrow |11\rangle$, $|01\rangle \leftrightarrow |12\rangle$, $|10\rangle \leftrightarrow |21\rangle$ are processes that simultaneously absorb or emit two photons, thus, have largely off-resonant transition frequencies providing small corrections. (iii) The interaction between two computational states |01\rangle and |10\rangle shifts the state energies with nearly equal magnitudes in opposite directions making small contribution to the ZZ conditional phase $\zeta = \phi_{00} +$ $\phi_{11} - \phi_{01} - \phi_{10}$. Therefore, the overall conditional phase ζ is mainly determined by the phase accumulation for state [11]. This allows us to implement the CZ gate by a closeto-resonance 2π rotation between the states [11] and one of the states |02) or |20). We find consistently high-fidelity CZ gate across different couplings J_C , as shown in Fig. 2 for 10 MHz $\leq J_C/h \leq$ 15 MHz.

We also analyze the unitary error budget for the CZ gate. The phase error is modeled as an extra phase $\delta\phi$ on the ZZ phase by $\zeta = \pi + \delta\phi$. When no leakage is present, the phase error is approximately $3(\delta\phi)^2/20$, according to Eq. (12). The leakage error is modeled as a leakage in the |11\rangle state $\hat{U}|11
angle = -\cos\epsilon |11
angle + i\sin\epsilon |02
angle$, which gives an error to be approximately $\sin^2(\epsilon)/4$ by Eq. (12). There could also be unwanted rotation between |01\rangle and |10\rangle states, which we model as $\hat{U}|01
angle = \cos\gamma |01
angle + i\sin\gamma |10
angle$, and similarly for |10\rangle state. The rotation error is approximately $2\sin^2(\gamma)/5$.

As Fig. 2 shows, the leakage error is the dominant contribution to the total error. The rotation error is a few orders of magnitude smaller than the leakage and total error but then increases to around 5×10^{-7} as J_C increases. The

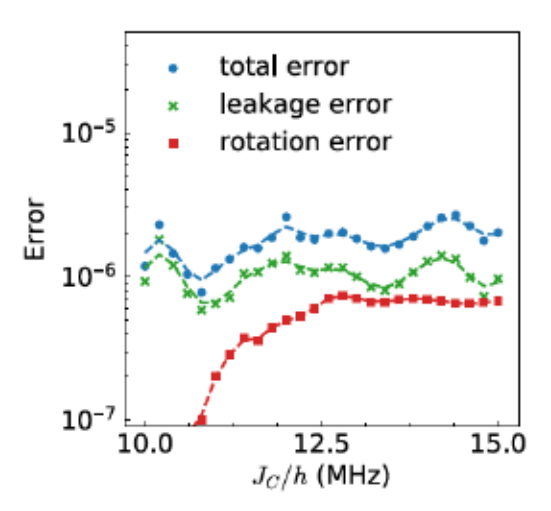


FIG. 2. The total coherent error of the CZ gate (blue dots), together with estimates of the leakage error (green crosses) and rotation error (red squares). The dashed lines correspond to smooth fits and are drawn for visual clarity. The qubit parameters are chosen to be $E_{C,F}/h = E_{C,T}/h = 0.2$ GHz, $E_{J,F}/E_{C,F} = 100$, $E_{J,T}/E_{C,T} = 78$.

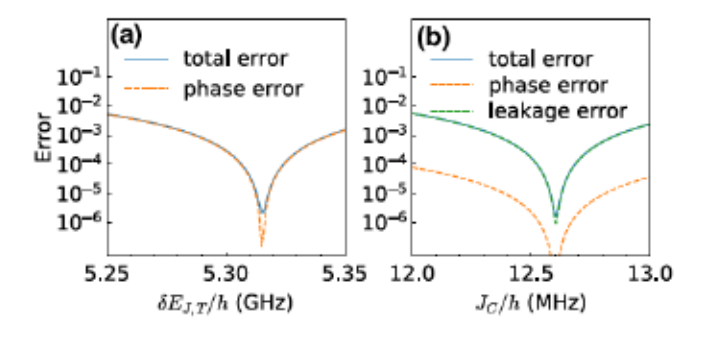


FIG. 3. The coherent error of CZ gate (blue solid) under the variation of (a) the drive amplitude $\delta E_{J,T}$ and (b) coupling constant J_C , decomposed into the phase error (orange dashed) and leakage error (green dashed). The pulse parameters are optimized at $J_C/h = 12.6$ MHz, as in Fig. 2.

phase error contributes the least, mostly around or below 10^{-7} , and thus is not shown in the plot. This low phase error has a simple interpretation. The CZ gate is based on a geometric phase induced by the pulse and this geometric phase could be easily tuned by choosing a slightly different trajectory on the 11-02 Bloch sphere to account for additional spurious contributions the conditional phase. For example, the drive can be chosen slightly off resonance to account for extra phases accumulated by other states.

We note that the fluctuations of the leakage error and the phase error are mainly the results of how the numerical optimization algorithm finds the optimal fidelity rather than some intrinsic mechanism of the gate. The total error of the CZ gate overall is consistently less than 10^{-5} , which is below the threshold to perform error-correction codes that use CZ gates to build stabilizer sequences, e.g., the distance-three code [46].

In Fig. 3 we show the sensitivity of the CZ gate fidelity to the variations of the drive amplitude δE_J and the coupling constant J_C . The pulse parameters used are optimized at $J_C/h = 12.6$ MHz as in Fig. 2. Note that to keep error below 10^{-3} , $\delta E_J/h$ can be allowed to vary within an approximately 60 MHz interval, while the variation of J_C can be no more than approximately 0.5 MHz. The variation of $\delta E_{J,T}$ mainly affects the phase error, while the leakage error varies around or below 10^{-5} , thus is not shown in the plot. For the variation of J_C , on the other hand, the leakage error dominates.

IV. THE iSWAP GATE

The *i*SWAP gate is another type of two-qubit entangling gate that, combined with single-qubit gates, is sufficient for universal quantum computation [47]. This gate is compromised by the parasitic ZZ phase accumulation, and processes for eliminating such parasitic phases has been a key aspect for implementing high-fidelity *i*SWAP gate [14,27,48]. The *i*SWAP gate requires a complete swapping process between |01⟩ and |10⟩, thus the modulation

frequency ω_p should satisfy the resonance condition $\omega_p = \Delta$ of \hat{H}_{iSWAP} in Eq. (8a). This requirement also means that the pulse should perform a complete π rotation in the subspace spanned by $|01\rangle$ and $|10\rangle$, which implies $g_{01,10}t_{gate} \simeq \pi$, where t_{gate} is the gate time or the length of the pulse. Thus the range of pulse parameters is rather restricted. As a result, the extra phase on $|11\rangle$ state due to phase ζ accumulation, see Eq. (9), cannot be easily compensated by optimization of the pulse.

In Fig. 4 we show the simulation result for implementing an *i*SWAP gate with the same qubit parameters as in Sec. III, except that we show the result for two different $\bar{E}_{J,T}$. As the top panel demonstrates, the infidelity curves have deep valleys for both cases but are clearly less than ideal when J_C is away from the valley. The main contribution to the gate error is the phase error, as demonstrated by the bottom panel, where the ZZ phase for the optimized gate is plotted against J_C . The valleys for fidelity curves happen right at the points where the ZZ phase error crosses zero. As a numerical comparison, we model the error of incomplete rotation between $|01\rangle$ and $|10\rangle$ as $\hat{U}|01\rangle = \sin \gamma |01\rangle + i\cos \gamma |10\rangle$ and vice versa. The rotation error then again can be estimated by $2\sin^2(\gamma)/5$. The

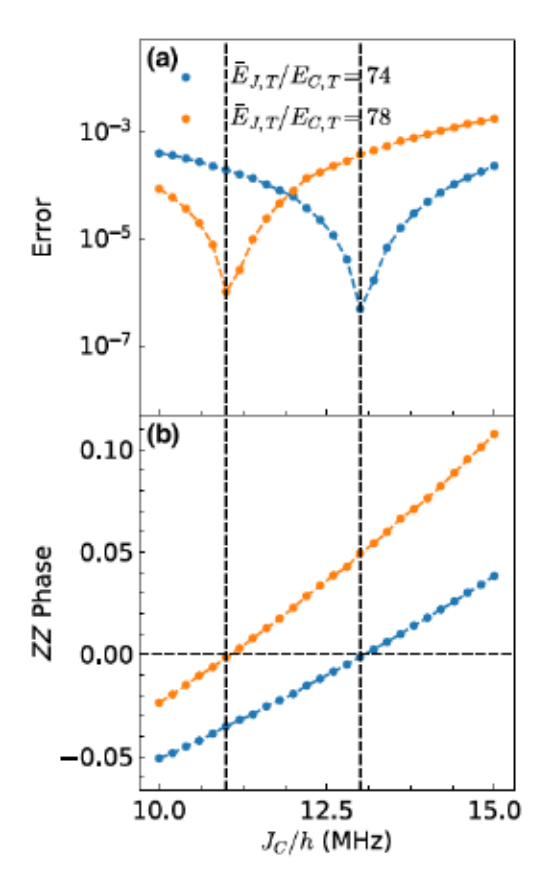


FIG. 4. Simulation results for *i*SWAP gate for $E_{J,T}/E_{C,T} = 74$ (blue) and $E_{J,T}/E_{C,T} = 78$ (orange). (a) The total coherent error of *i*SWAP gate. (b) ZZ phase accumulated during the *i*SWAP operation. The dashed lines are smooth fittings.

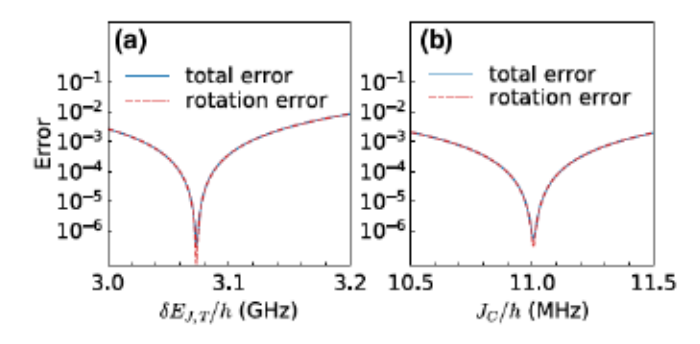


FIG. 5. The total coherent error (blue solid) of iSWAP gate under the variation of (a) $\delta E_{J,T}$ and (b) J_C , compared with the rotation error (red dashed). The gate parameters are optimized at $J_C/h = 0.011$ GHz for $\bar{E}_{J,T}/E_{C,T} = 78$, as in Fig. 4.

phase error, on the other hand, is modeled as an extra phase on $|11\rangle$ state $\hat{U}|11\rangle = e^{i\delta\phi}|11\rangle$, and by Eq. (12), it contributed approximately $3(\delta\phi)^2/20$ to the total error. Our numerical evaluation shows that the rotation error is several orders of magnitude less than the total error, except at the dip of the error curve, thus we do not show the rotation error in Fig. 4. The phase error, on the other hand, is nearly indistinguishable from the total error, and thus is also not displayed in the plot.

The unconditional phase ζ mostly comes from the off-resonant state $|00\rangle$ and $|11\rangle$, $\zeta = \phi_{00} + \phi_{11}$. In Appendix B, we provide a perturbative estimate for such a phase, which captures the main contribution to ZZ coupling. The corrections depend on the static energy spectrum and thus can be controlled by the static Josephson energy $E_{J,T}$ of the tunable qubit. In Fig. 4, we show the comparison of iSWAP gate for different $E_{J,T}$ in the range of 10 MHz $\leq J_C/h \leq$ 15 MHz. As demonstrated by the top panel, the infidelity curves now have the valleys at a different coupling J_C . In the bottom panel, the change in $E_{J,T}$ correspondingly induces changes in the slope and offset of the ZZ phase curve, thus also changing the point where the curve crosses zero. Therefore, a ZZ-free iSWAP gate can be achieved by tuning the static Josephson energy $E_{J,T}$ of the tunable qubit, which can be implemented in situ by tuning the gate voltage.

In Fig. 5 we again show the sensitivity of gate fidelity to the system parameters. The pulse parameters are optimized at $J_C/h = 11$ MHz for $\bar{E}_{J,T}/E_{C,T} = 78$, as in Fig. 4. The infidelity of *i*SWAP gate can be kept below 10^{-3} if the drive amplitude variates within a range of approximately 60 MHz, and if J_C variation within of range of approximately 0.6 MHz. The gate error due to sensitivity is dominated by the rotation error.

V. THE √iSWAP GATE

Here we provide simulations of \sqrt{i} SWAP gate. While the gate fidelity is also limited by an error due to an unwanted

conditional phase ζ , for a $\sqrt{i\text{SWAP}}$ gate, a complete swap between states $|01\rangle$ and $|10\rangle$ is no longer necessary as only a swap probability of 1/2 is needed. This loosens the restriction on the pulse parameters, and it is possible to correct the ZZ phase by simply adjusting the pulse parameters. We find two ways to design the pulse shape: (i) a one-tone pulse that performs an off-resonant Rabi oscillation and (ii) a two-tone pulse that combines two sinusoidal pulses, with modulation frequency offset by some small value. For the error budget, we define the phase error is modeled and calculated in the same way as that for iSWAP gate, so it is estimated by $3(\delta\phi)^2/20$. We model the rotation error as

$$\hat{U}|01\rangle = \cos\left(\frac{\pi}{4} + \gamma\right)|01\rangle + i\sin\left(\frac{\pi}{4} + \gamma\right)|10\rangle$$

where ϵ can be positive or negative, and similar error model holds for state |10⟩. The rotation error is then approximately $3\sin^2(2\gamma)/20$. Since it is second-order effect, it is not the major error mechanism for $\sqrt{i\text{SWAP}}$ gate. We also include the leakage error $\hat{U}|11\rangle = \cos \epsilon |11\rangle + \sin \epsilon |02\rangle$, which approximately contributes $9\sin^2(\epsilon)/40$ to the total error.

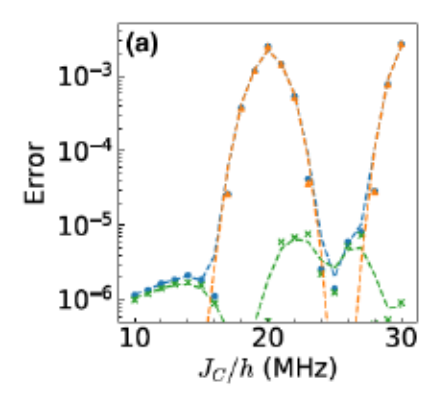
A. One-tone pulses

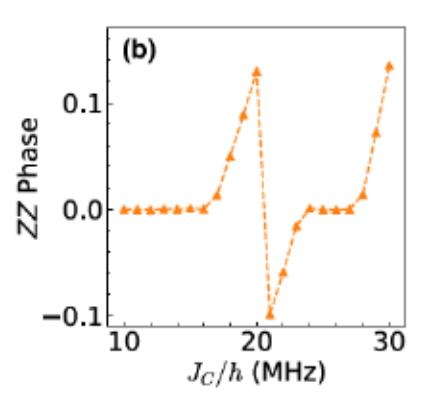
A one-tone pulse may achieve the $\sqrt{i\text{SWAP}}$ gate by an off-resonant Rabi oscillation. In the reduced subspace spanned by $|01\rangle$ and $|10\rangle$, the unitary evolution matrix describes the Rabi oscillations, see Eq. (C1). The $\sqrt{i\text{SWAP}}$ gate requires the unitary matrix to have magnitude $1/\sqrt{2}$ in all entries, including the off-diagonal elements

$$\frac{g_{01,10}}{\sqrt{g_{01,10}^2 + \delta^2}} \sin\left(\frac{1}{2}\sqrt{g_{01,10}^2 + \delta^2} t_{\text{gate}}\right) = \pm \frac{1}{\sqrt{2}}, \quad (13)$$

where $g_{01,10}$ is the effective coupling between $|01\rangle$ and $|10\rangle$ states, and $\delta = \omega_p - \Delta$ is the frequency detuning. This equation depends on the effective coupling $g_{01,10}$ and is not always satisfied. The off-resonant Rabi oscillation also introduces extra phases on the off-diagonal terms, but this does not change the ZZ phase in the local-equivalent form, see Appendix C. Nevertheless, the off-resonant case introduces change into the $g_{01,10}$ term, which then changes the offset of ZZ phase-accumulation rate as already explained for the iSWAP gate. Thus, it is possible to correct the ZZ phase error for \sqrt{i} SWAP gate by only changing the pulse parameters.

Figure 6(a) shows the simulation result of $\sqrt{i\text{SWAP}}$ gates using one-tone pulses, with coupling J_C ranging from 10 to 30 MHz. The ZZ phase curve now has a plateau of zero phase error, rather than a single-point intersection with the J_C/h axis, as shown by Fig. 6(b). The endpoints of the zero plateau correspond to two types of extrema for the ZZ phase, one happens close to resonance, and the other





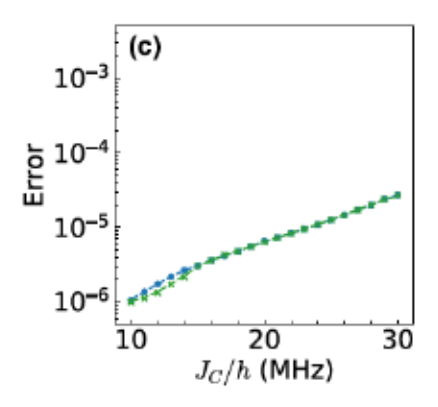


FIG. 6. The simulation results for one-tone and two-tone pulses $\sqrt{i\text{SWAP}}$ gate. The dashed lines are smooth fittings. (a) The error for one-tone $\sqrt{i\text{SWAP}}$ gate. The total error (blue dots) is decomposed into phase error (orange triangles) and leakage error (green crosses). (b) The conditional phase ζ of the one-tone gate is presented in (a). The phase vanishes in a broad range of J_C , but cannot be reduced for other intervals of J_C , resulting in strong enhancement of the gate error in these intervals, cf. panel (a). (c) The error for two-tone $\sqrt{i\text{SWAP}}$ gate. The total gate error (blue dots) remains small in the whole interval of J_C and is dominated by leakage error (green crosses). The qubit parameters are the same as in Fig. 2 or Fig. 4.

is related to the parameter $g_{01,10}$. In the plateau region, the phase error is insignificant, and the error is dominated by the leakage error out of the computational subspace. On the other hand, in the parameter range outside the plateau, the ZZ phase deviates from zero, and the error curve has peaks. The error budget shows that the major contribution of error along the peaks comes from the phase error. Also, there is a discontinuity of ZZ phase error at $J_C = 20$ MHz, which corresponds to the discontinuity in the pulse parameters. This discontinuity is related to the choice of a different branch of the Rabi-oscillation period when the swapping process switches from a $3\pi/2$ rotation to a $5\pi/2$ rotation; the detail of the analysis above can be found in Appendix D.

B. Two-tone pulses

Another way to correct the ZZ phase error is to composite two pulses with close but different modulation frequencies, so that the combined pulse is

$$E_{J,T}(t) = \bar{E}_{J,T}$$

$$+ f(t)(\delta E_{J,T,1} \cos(\omega_{p,1}t) + \delta E_{J,T,2} \cos(\omega_{p,2}t)). \tag{14}$$

This introduces alternative pulse parameters, adding more degree of freedom for ZZ phase elimination. As shown in Fig. 6(c) for J_C/h ranging form 10 to 30 MHz, the two-frequency method can correct the ZZ phase error more efficiently, restricting the ZZ phase error to have amplitude $<10^{-3}$. We optimize only the driving amplitudes of the two-tone pulses, but keep modulation frequencies $\omega_{p,1}$ and $\omega_{p,2}$ fixed across different J_C . The reason for this is to simplify the optimization procedure, but as Fig. 6(c) shows, although the infidelity increases monotonically with J_C , it can be kept $<10^{-4}$ across this range of J_C , thus our way

to optimize only driving amplitudes can still be justified. The monotonic increase is mainly the result of increasing leakage of $|11\rangle$ state, which increases from the order of 10^{-6} to the order of 10^{-4} as J_C increases from 10 to 30 MHz, while the other error mechanisms, including the phase error, contribute below 10^{-7} to the total error, several orders of magnitude less than the leakage error. This increase in leakage is due to the increasing coupling constant J_C , which also increases the coupling between $|11\rangle$ and $|02\rangle$ state.

VI. EFFECT OF DECOHERENCE ON GATES

The results in the previous sections were obtained for unitary system evolution. For physical qubits, we also need to take the decoherence process into consideration. Therefore, we also use the same qubit and pulse parameters to simulate the following master equation with finite relaxation times:

$$\dot{\hat{\rho}}(t) = -\frac{i}{\hbar} \left[\hat{H}(t) \right] \hat{\rho}(t) + \sum_{\alpha = F, T} \frac{1}{T_{1,\alpha}} \mathcal{D}_{\alpha}(\hat{\rho}(t)). \tag{15}$$

Here $\hat{H}(t)$ is the two-qubit Hamiltonian defined as in Eq. (1), and the superoperator \mathcal{D}_{α} is defined as

$$\mathcal{D}_{\alpha}(\hat{\rho}) = \sum_{j=0}^{J_{t}} 2\hat{c}_{\alpha,j} \hat{\rho} \hat{c}_{\alpha,j}^{\dagger} - \hat{\rho} \hat{c}_{\alpha,j}^{\dagger} \hat{c}_{\alpha,j} - \hat{c}_{\alpha,j}^{\dagger} \hat{c}_{\alpha,j} \hat{\rho}$$

$$\hat{c}_{F,j} = \sqrt{j+1} \sum_{i} |j,i\rangle \langle j+1,i| \qquad (16)$$

$$\hat{c}_{T,j} = \sqrt{j+1} \sum_{i} |i,j\rangle \langle i,j+1|.$$

The $T_{1,\alpha}$ stands for the relaxation times of each qubit, and for convenience, we will set $T_{1,F} = T_{1,T}$ in simulations.

Here j_t is the truncation number of states. For $t_{\text{gate}} \ll T_1$, we expect that the fidelity F will follow an exponential relation with respect to the gate time, so $1 - F \simeq 4t_{\text{gate}}/5T_1$ (assuming that $T_2 = 2T_1$) [49]. For example, the error for both gates around $T_1 = 100 \ \mu s$ is around 6×10^{-4} , close to the theoretical prediction. The simulated fidelity F is calculated with process fidelity F_p and chi matrix χ of the process by $F = [4F_p + \text{Tr}(\chi)]/5$ [50].

In Fig. 7 we show the simulation results with dissipation for both CZ gate and iSWAP gate, using parameters for Figs. 2 and 4 at $J_C/h = 10$ MHz. We also simulate for both one-tone and two-tone \sqrt{i} SWAP gate, which is not shown in the plot because the curves of $\sqrt{i}SWAP$ gate fidelity and iSWAP gate fidelity as a function of T_1 are nearly indistinguishable on the plot. We note that for fault-tolerant error-correction code, the plot suggests that T_1 should be greater than 10 μ s to achieve the reported threshold error rate 0.57% for surface code [51]. In truth, several experiments that use typical transmon qubits to implement surface code report T_1 's that are above this threshold [52,53]. However, if we aim for higher fidelity that surpasses 0.1%, we need at least $T_1 \gtrsim 70 \ \mu s$. Recent nanowire gatemons have seen an improvement of T_1 to over 20 µs [54], which would satisfy the former threshold, but still needs to be further improved to pass the latter. Therefore, understanding the decoherence mechanism and improving the qubit coherence should be a crucial part for development of gatemon-based quantum processors.

The above estimate of nonunitary error on the entangling gates is made for 75-ns gate time for the case of $T_2=2T_1$ (no extra dephasing rate due to gate-voltage fluctuations). This estimate gives the $T_1 \gtrsim 70~\mu s$ threshold as a lower bound to achieve 99.9% fidelity in entangling gates. In reality, T_2 may be shorter than $2T_1$ or system parameters

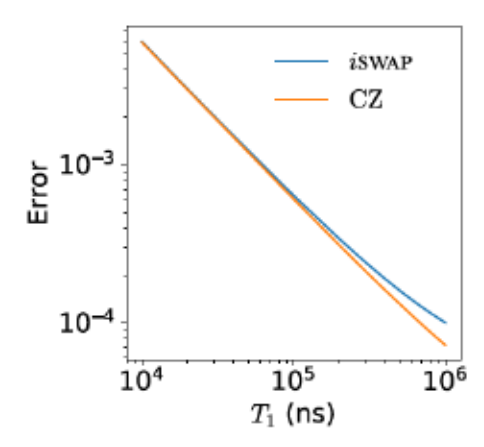


FIG. 7. Simulations with dissipation for CZ and *i*SWAP gates. The qubit and pulse parameters are the same as in Figs. 2 and 4, with $J_c/h = 10$ MHz. As T_1 approaches 1 ms, the gate error for *i*SWAP saturates towards its unitary estimate of approximately 8×10^{-5} , which is higher than that estimate for the CZ gate (approximately 10^{-6}).

may require longer gate times, both leading to even longer T_1 time requirements.

VII. CONCLUSION

We described implementation of parametric entangling gates on superconductor-semiconductor hybrid qubits using voltage modulation pulses. We simulate CZ gate, iswap gate, \sqrt{iswap} with this idea, and demonstrate that all gates can have coherent error <10⁻⁵, with proper choice of qubit and pulse parameters. In particular, the CZ gate has the least stringent conditions and does not require an extra procedure to correct the accumulated ZZ phase. The iSWAP gate, on the other hand, is mainly limited by the ZZ phase but can be corrected by tuning the static Josephson energy, which changes the offset of the ZZ phase curve by an ac-Stark shift term. The \sqrt{i} SWAP has less stringent conditions than the iSWAP gate, thus can be partially corrected by choice of pulse parameters alone. Using one-tone pulses, the conditional ZZ phase can be corrected in a finite range, unlike that in the iSWAP case where the correctable static ZZ phase has to be equal to the offset determined by the qubit parameters. For two-tone pulses, the ZZ phase accumulation can be corrected in a wider range of qubit parameters by tuning the pulse amplitudes only, in this case, the gate performance is limited by leakage errors.

We also simulate the sensitivity of the gate fidelity to the variations of the drive amplitude and the coupling constant. We find that to keep the coherent error below 10^{-3} , the variation of $\delta E_{J,T}$ should be no more than 60 MHz for both CZ and *i*SWAP gate, while the variation of J_C should be no more than 0.5 MHz for CZ gate, and no more than 0.6 MHz for *i*SWAP gate. For decoherence, we find that to have fault-tolerant gates ready for error correction, we need $T_1 > 70~\mu s$. The current state-of-the-art superconductor-semiconductor hybrid qubits fall short of this demand, but our simulation may set a standard for future improvements in hardware.

Although the coherence of gatemon qubit is still less than ideal, future advancement in hardware fabrication can alleviate such a limit and extend gatemon's T_1 to be above the threshold mentioned earlier. Further investigation of superconducting-semiconducting hybrid structures could bring fruitful results for developing voltage-controlled superconducting circuits, such as gatemon qubits and tunable resonators [55].

ACKNOWLEDGMENT

The authors acknowledge support from the Army Research Office Agreement No. W911NF2110303. We performed computations using resources and assistance of the UW-Madison Center For High Throughput Computing (CHTC) in the Department of Computer Sciences. The CHTC is supported by UW-Madison, the Advanced Computing Initiative, the Wisconsin Alumni Research Foundation, the Wisconsin Institutes for Discovery, and the National Science Foundation.

APPENDIX A: INTERACTION HAMILTONIAN

To derive a more complete Hamiltonian, we follow the method presented in Ref. [19], but make changes to fit our model. Define the variable $\xi_i = \sqrt{2E_{CJ}/E_{J,i}}$, where i = F, T. With the transformation into instantaneous eigenbasis of single qubit, we may write the truncated Hamiltonian as [19]

$$\hat{H}_{M}(t) = \sum_{i=0}^{2} [\nu_{F,i} \hat{\Pi}_{F,i} + \nu_{T,i}(t) \hat{\Pi}_{T,i}]$$

$$+ g(t) [\lambda_{F} \hat{\sigma}_{F,01}^{y} + \sqrt{2} \Lambda_{F} \hat{\sigma}_{F,12}^{y}] [\lambda_{T}(t) \hat{\sigma}_{T,01}^{y}$$

$$+ \sqrt{2} \Lambda_{T}(t) \hat{\sigma}_{T,12}^{y}] + \mu(t) \hat{\sigma}_{T,02}^{y},$$
(A1)

where $\hat{\Pi}_{n,i}$ is projection operator of nth single-qubit eigenstate, and $\hat{\sigma}_{Q,ij}^{y}$ stands for the Pauli y matrix between single-qubit states $|i\rangle$ and $|j\rangle$ for qubit Q. The coefficients λ_{i} and Λ_{i} are determined by ξ_{i} , but in the transmon regime, they are close to unity. The notation $\nu_{Q,i}(t)$ stands for the instantaneous frequencies of qubit Q, and we use

$$\omega_{O,ij}(t) = \nu_{O,i} - \nu_{O,i} \tag{A2}$$

to denote the single-qubit instantaneous transition frequency. The coupling g is defined by,

$$g(t) = J_C/(4\sqrt{\xi_F \xi_T(t)}),$$
 (A3)

and

$$\mu(t) = \langle 0_T(t) | \frac{d}{dt} | 2_T(t) \rangle.$$
 (A4)

Here $|i(t)\rangle$ is the *i*th eigenstate for the time-dependent Hamiltonian. The 0 to 2 transition term is present in the interaction picture because of the $\hat{\varphi}^2$ perturbation after expanding the cos term in the single qubit Hamiltonian. Also, for the combined system, we use the notation,

$$v_{ii}(t) = v_{F,i} + v_{T,i}(t),$$
 (A5)

and denote the two-qubit transition frequencies as

$$\omega_{ij,rs}(t) \equiv v_{rs}(t) - v_{ij}(t). \tag{A6}$$

Now assume a periodic modulation with frequency ω_p on the tunable qubit. This means that we can write down the instantaneous eigenfrequencies for the tunable qubit as a Fourier series

$$v_{T,i}(t) = \sum_{m=0}^{\infty} v_{m;T,i} \cos(m\omega_p t), \quad (A7)$$

and similarly for $\omega_{T,ij}(t)$, $\nu_{ij}(t)$, and $\omega_{ij,rs}(t)$. Before transform to interaction picture, we first need the Jacobi-Auger identity, which states that $e^{tx \sin y} = \sum_{l=-\infty}^{\infty} J_n(x)e^{iny}$, where J_n is the Bessel function of first kind. Then,

$$e^{i\int_0^t dt' \omega_{ij,rs}(t)} = e^{if_0t} \sum_{n \in \mathbb{Z}} G_n(\{\omega_{k;rs,ij}\}) e^{in\omega_p t}$$

$$\{\omega_{k;rs,ii}\} = (\omega_{0;rs,ii}, \omega_{1;rs,ii}, \dots),$$
(A8)

the coefficient G_n is

$$G_n(\{\omega_{k;rs,ij}\}) = \sum_{(l_k) \in S_n} \left(\prod_{k=1}^{\infty} J_{l_k} \left(\frac{\omega_{k;rs,ij}}{k\omega_p} \right) \right),$$
 (A9)

where the set S_n of integer sequences is defined as

$$S_n = \left\{ (l_1, l_2, \ldots) | l_k \in \mathbb{Z}, \sum_{k=1}^{\infty} k l_k = n \right\}.$$
 (A10)

Now transform the Hamiltonian \hat{H}_M into the interaction picture with the unitary matrix

$$\hat{U}_{int} = \exp{-i\int_0^t dt' \sum_{i=0}^2 [\nu_{F,i} \Pi_{F,i} + \nu_{T,i} \Pi_{T,i}]}, \quad (A11)$$

which eliminates the diagonal element. With the notation above, the matrix elements then transform as

$$\hat{U}_{\text{int}} |ij\rangle \langle rs| \, \hat{U}_{\text{int}}^{\dagger}$$

$$= e^{i(\omega_{0,rs} - \omega_{0,ij})t} \sum_{n \in \mathbb{Z}} G_n(\{\omega_{k;rs,ij}\}) e^{in\omega_p t} |ij\rangle \langle rs|. \quad (A12)$$

From the off-diagonal terms in $H_M(t)$, we expect that

$$H_{\text{int}}(t) = \sum_{n \in \mathbb{Z}} \sum_{ij,rs} g_{ij,rs}^{(n)}(t) e^{i(\omega_{0,rs} - \omega_{0,ij} + n\omega_{p})t}$$

$$+ \sum_{n \in \mathbb{Z}} \Omega_{02}^{(n)}(t) e^{i(n\omega_{p} + 2\bar{\omega}_{T,01} - \bar{\eta}_{T})t} I_{3} \otimes |2\rangle \langle 0| + \text{h.c.},$$
(A13)

where n runs over all the integers. The coupling coefficients and resonant frequencies for are

$$g_{00,11}^{(n)}(t) = -g(t)\lambda_{F}\lambda_{T}(t)G_{n}(\{\omega_{k;11,00}\}), \qquad \omega_{0;11,00} = \omega_{F,01} + \bar{\omega}_{T,01};$$

$$g_{01,10}^{(n)}(t) = g(t)\lambda_{F}\lambda_{T}(t)G_{n}(\{\omega_{k;10,01}\}), \qquad \omega_{0;10,01} = -\omega_{F,01} + \bar{\omega}_{T,01};$$

$$g_{11,22}^{(n)}(t) = -2g(t)\Lambda_{F}\Lambda_{T}(t)G_{n}(\{\omega_{k;22,11}\}), \qquad \omega_{0;22,11} = \omega_{F,01} + \bar{\omega}_{T,01} - \eta_{F} - \bar{\eta}_{T};$$

$$g_{12,21}^{(n)}(t) = 2g(t)\Lambda_{F}\Lambda_{T}(t)G_{n}(\{\omega_{k;21,12}\}), \qquad \omega_{0;21,12} = \omega_{F,01} - \bar{\omega}_{T,01} - \eta_{F} + \bar{\eta}_{T};$$

$$g_{01,12}^{(n)}(t) = -\sqrt{2}g(t)\lambda_{F}\Lambda_{T}(t)G_{n}(\{\omega_{k;12,01}\}), \qquad \omega_{0;12,01} = \omega_{F,01} + \bar{\omega}_{T,01} - \bar{\eta}_{T};$$

$$g_{02,11}^{(n)}(t) = \sqrt{2}g(t)\lambda_{F}\Lambda_{T}(t)G_{n}(\{\omega_{k;21,10}\}), \qquad \omega_{0;21,10} = \omega_{F,01} + \bar{\omega}_{T,01} - \eta_{F};$$

$$g_{10,21}^{(n)}(t) = -\sqrt{2}g(t)\Lambda_{F}\lambda_{T}(t)G_{n}(\{\omega_{k;21,10}\}), \qquad \omega_{0;21,10} = \omega_{F,01} + \bar{\omega}_{T,01} - \eta_{F};$$

$$g_{11,20}^{(n)}(t) = \sqrt{2}g(t)\Lambda_{F}\lambda_{T}(t)G_{n}(\{\omega_{k;20,11}\}), \qquad \omega_{0;20,11} = \omega_{F,01} - \bar{\omega}_{T,01} - \eta_{F};$$

and

$$\Omega_{02}^{(n)}(t) = \mu(t)G_n(\{\omega_{k;T,02}\}), \quad \omega_{0;T,02} = 2\bar{\omega}_{T,01} - \bar{\eta}_T.$$
(A15)

Although the expression for G_n complicated, for weak modulation on the system spectrum, the leading contribution to G_n can be simplified to the Bessel function $J_n(\omega_{1:ij,\ell'j'}/\omega_p)$, where $\omega_{1:ij,i'j'}$ is the amplitude of frequency modulation to the harmonic mode, which is determined by the Josephson modulation amplitude in the actual system. In particular, for n=0,

$$G_0(\{\omega_{k;ij,i'j'}\}) \approx J_0\left(\frac{\omega_{1;ij,i'j'}}{\omega_p}\right),$$
 (A16)

and for n = 1,

$$G_1(\{\omega_{k;ij,i'j'}\}) \approx J_1\left(\frac{\omega_{1;ij,i'j'}}{\omega_p}\right).$$
 (A17)

When the modulation is weak, we can further simplify by the approximation $J_0(\omega_{1;ij,j'j'}/\omega_p) \approx 1$ and $J_1(\omega_{1;ij,j'j'}/\omega_p) \approx \omega_{1;ij,j'j'}/2\omega_p$. For g(t) that is nearly constant under weak modulation, the n=0 terms then roughly correspond to the static Hamiltonian, and the n=1 terms correspond to the drive Hamiltonian as presented in Eqs. (8).

For the qualitative analysis below, we will assume $g^{(n)}$ to be constant for convenience.

APPENDIX B: QUALITATIVE ANALYSIS ON PHASE ACCUMULATION FOR OFF-RESONANT STATES

The unitary operator used in Eq. (A11) is essentially a single-qubit operation. Therefore, to analyze the ZZ phase

due to the evolution, it is sufficient to look at the interaction Hamiltonian (A13). For convenience, let us denote the two-qubit state by a single letter k, l, etc. We can write the relevant two-qubit term as,

$$H_r = \sum_{n} \sum_{k \neq l} g_{kl}^{(n)} |k\rangle \langle l| e^{i\omega_{kl}^{(n)}t}, \tag{B1}$$

with the summation of n runs over all integers. Here we assume $g_{kl}^{(n)} = g_{kl}^{(-n)}$ are real effective coupling between states $|k\rangle$ and $|l\rangle$ for each mode n, and $\omega_{kl}^{(n)} = -\omega_{kl}^{(-n)} = \omega_{0;l} - \omega_{0;k} + n\omega_{p}$, with notation as in Appendix A. Thus we have the relation,

$$\omega_{lr}^{(n)} + \omega_{rk}^{(n')} = \omega_{kl}^{(n+n')}$$
 (B2)

Suppose the system state is $\psi(t) = \sum c_k |k\rangle$. The time evolution of the state then satisfies the first-order time differential equation:

$$\dot{c}_l = \sum_{n \in \mathbb{Z}} \sum_k -i g_{lk}^{(n)} e^{i\omega_{lk}^{(n)} t} c_k.$$
 (B3)

This linear differential equation is not easy to solve. However, since the Hamiltonian is bounded and Lipschitz, it is reasonable to assume that the recursion relation:

$$\psi^{(i+1)}(t) = \psi(0) - i \int_0^t H_r(t') \psi^{(i)}(t') dt'$$
 (B4)

converges to a fixed point [56]. With RWA, by choosing a proper $\psi^{(0)}$, we can assume that the recursion converges rapidly, thus giving us a good estimate within a few recursive steps.

Now assume that the initial state is $\psi(0) = |k\rangle$, such that no $\omega_{kl}^{(n)}$ is close to 0. Suppose also that $\left|\omega_{ll'}^{(n)}\right| \gg |g_{ll'}|$ for all

l, l' in concerns, and the terms with $\omega_{ll'}^{(n)} \approx 0$ do not contribute. In this case, we expect that $\psi(t)$ does not deviate

from $|k\rangle$ too much by the RWA assumption. Thus we have $c_k^{(0)} = 1$, and

$$c_{l}^{(2)} = -\sum_{n \in \mathbb{Z}} \frac{g_{lk}^{(n)}}{\omega_{lk}^{(n)}} (e^{i\omega_{lk}^{(n)}t} - 1) + \sum_{n, n' \in \mathbb{Z}} \sum_{l' \neq l, k} \frac{g_{l'k}^{(n)} g_{l'}^{(l)}}{\omega_{l'k}^{(n)}} \left(\frac{1}{\omega_{ll'}^{(n+n')}} (e^{i\omega_{kl'}^{(n+n')}t} - 1) - \frac{1}{\omega_{ll'}^{(l)}} (e^{i\omega_{ll'}^{(l)}} - 1) \right) \quad l \neq k$$

$$c_{k}^{(2)} = 1 + \sum_{n \in \mathbb{Z}} \sum_{k \neq l} \frac{\left| g_{lk}^{(n)} \right|^{2}}{\omega_{lk}^{(n)}} it + \sum_{n \neq n' \in \mathbb{Z}} \sum_{k \neq l} \frac{g_{lk}^{(n)} g_{lk}^{(n')}}{\omega_{lk}^{(n)} (n-n')\omega_{p}} (e^{i(n-n')\omega_{p}t} - 1) + \sum_{n,n' \in \mathbb{Z}} \sum_{k \neq l} \frac{g_{lk}^{(n)} g_{kl'}^{(n')}}{\omega_{lk}^{(n)} \omega_{kl'}^{(n')}} (e^{i\omega_{kl'}^{(n')}t} - 1).$$
(B5)

Let

$$\epsilon = \max_{n,l \neq l'} \left\{ \left| \frac{g_{l,l'}^{(n)}}{\omega_{l,l'}^{(n)}} \right|, \frac{g_{l,l'}^{(n)}}{\omega_p} \right\}, \quad (B6)$$

the largest correction then is present in the $|c_n^{(2)}|$ term as linear in time t. Thus, to the leading order of ϵ , the phase accumulation rate of c_k is approximately

$$\phi_k/t \approx \sum_n \sum_l \frac{\left|g_{lk}^{(n)}\right|^2}{\omega_{lk}^{(n)}}.$$
 (B7)

We note that for such approximation to hold, $g_{l,l'}^{(n)}$ should be consistently smaller than $\omega_{l,l'}^{(n)}$ when there is no resonance between m and m'. We argue from Eq. (A9) that $g_{l,l'}^{(n)}$ has a leading term $J_m(\omega_{1;l,k})_1/\omega_p$), which asymptotically is restricted by

$$\frac{1}{m!} \left(\frac{\omega_{1;l,k}}{2\omega_p} \right)^m$$

for $\omega_{1:l,k}/\omega_p \ll \sqrt{m+1}$ [57]. Therefore, we expect the contribution from higher m modes to be small enough, and focus only on the order of magnitudes for lower m modes. In particular, we are using m = 1 mode to build the gate, so the main concern is for the k = 0 and k = 1 modes. For concreteness, in Table II we show an example of relevant transition frequencies for the chosen qubit parameters. The qubit parameters are the same as those used for simulation, with $J_C = 10$ MHz. Using the static spectrum as a reference, we expect that for m = 0 mode, $\omega_{m;l,k}$ has the lower bound to be about 0.5 GHz. For m = 1 mode, we are concerned with the magnitude of $\omega_{m;l,k} - \omega_p$, where ω_p should be close to transition frequency of either $01 \leftrightarrow 10$ or 11 ↔ 02. The lower bound is the difference between the transition frequency between $01 \leftrightarrow 10$ and $12 \leftrightarrow 21$, which is about 0.003 GHz, but since the states |12| and |21) are out of computational subspace, and there is no direct coupling that relates these two transition processes, we argue that this lower bound should not have a significant contribution to the correction. The next lower bound is the difference between transition frequencies of $01 \leftrightarrow 10$ and $11 \leftrightarrow 02$ or $11 \leftrightarrow 20$, which is about 0.2 GHz. As a comparison, $g_{nn}^{(1)}$ should be of the order of π/t_{gate} , which for our choice of gate time is about 0.04 GHz. Thus, we argue that the approximation we make here should be reasonable for a rough estimate.

The m=0 term is approximately the static ZZ interaction rate found by second-order perturbation theory, and determines the slope in Fig. 4(b). The m=1 terms provide the ZZ phase a downward shift, and are similar to the ac Stark shift that is present in the off-resonant microwave method [2,3,58,59]. The difference is that in the microwave drive method, the numerator is the amplitude of the transverse drive, while here the numerator is given by Eq. (A14), which has a more complicated dependence on the pulse shape and modulation amplitude. As the iswap gate requires that $g_{01,10}^{(1)} = \pi/t_{\text{gate}}$, and all the other $g_{kl}^{(1)}$ should be proportional to $g_{01,10}^{(1)}$ as they correspond to the same harmonic mode, we see that the offset is then approximately

$$\sum_{k,l} \frac{\pi^2}{\omega_{k,l}^{(1)} t_{\text{gate}}} \left| \frac{g_{k,l}^{(1)}}{g_{01,10}^{(1)}} \right|^2 + \sum_{k,l} \frac{\pi^2}{\omega_{k,l}^{(-1)} t_{\text{gate}}} \left| \frac{g_{k,l}^{(1)}}{g_{01,10}^{(1)}} \right|^2.$$
(B8)

TABLE II. Relevant transition frequencies of the two-qubit system, calculated at $J_C = 10$ MHz.

Transition process	Transition frequency (GHz)	
00 ↔ 11	10.1058	
01 ↔ 10	0.7923	
11 ↔ 22	9.6635	
12 ↔ 21	0.7959	
02 ↔ 11	1.0151	
10 ↔ 21	9.8863	
11 ↔ 20	0.5734	

In summary, for off-resonant state $|ij\rangle$, the accumulation rate of ϕ_{ij} as determined by n = 0, I harmonic mode is

$$\frac{\phi_{ij}}{t_{\text{gate}}} \approx \sum_{kl \neq ij} \frac{(g_{ij,kl}^{(0)})^2}{\bar{\omega}_{kl} - \bar{\omega}_{ij}} + \sum_{kl \neq ij} \frac{2(\bar{\omega}_{kl} - \bar{\omega}_{ij})}{(\bar{\omega}_{kl} - \bar{\omega}_{ij})^2 - \omega_p^2} (g_{ij,kl}^{(1)})^2,$$
(B9)

where $\bar{\omega}_{ij}$ stands for the time average of corresponding frequency. As a demonstration, we compare the theoretical estimation and numerical result in Fig. 8. We use static $g^{(0)}$ for simplicity, and for $g^{(1)}$ terms, we estimate $g^{(0)}_{01,10}$ to be $\pi/t_{\rm gate}$ as mentioned before, then multiply by a factor of 1

or $\sqrt{2}$ for estimation of other terms based on the relations given in Eq. (A14). As the plot shows, although the theoretical estimation does not give a exact agreement, it still demonstrates the overall tendency of ZZ phase curve.

APPENDIX C: LOCAL EQUIVALENCE CLASS FOR √iswap GATE INDUCED BY ONE-TONE PULSES

In the reduced subspace of |01\(\) and |10\(\), the offresonant Rabi oscillation results in a unitary evolution of the form

$$\hat{U}_{\text{Rabi, off}} = \begin{pmatrix} e^{i\delta t_{\text{gate}}/2} \left[\cos \left(\frac{\Omega t_{\text{gate}}}{2} \right) - i \frac{\delta}{\Omega} \sin \left(\frac{\Omega t_{\text{gate}}}{2} \right) \right] & i e^{i\delta t_{\text{gate}}/2} \frac{g_{\text{eff}}}{\Omega} \sin \left(\frac{\Omega t_{\text{gate}}}{2} \right) \\ i e^{-i\delta t_{\text{gate}}/2} \frac{g_{\text{eff}}}{\Omega} \sin \left(\frac{\Omega t_{\text{gate}}}{2} \right) & e^{-i\delta t_{\text{gate}}/2} \left[\cos \left(\frac{\Omega t_{\text{gate}}}{2} \right) + i \frac{\delta}{\Omega} \sin \left(\frac{\Omega t_{\text{gate}}}{2} \right) \right] \end{pmatrix}, \quad (C1)$$

where $\Omega = \sqrt{g_{\text{eff}}^2 + \delta^2}$. Notice that the diagonal terms have exactly equal and opposite phases

$$\theta_{01} = -\theta_{10} = \frac{\delta t_{\text{gate}}}{2} - \arg \left[\cos \left(\frac{\Omega t_{\text{gate}}}{2} \right) - i \frac{\delta}{\Omega} \sin \left(\frac{\Omega t_{\text{gate}}}{2} \right) \right],$$
 (C2)

hence performing single qubit Z rotation on both qubits by equal and opposite angles θ_{01} and θ_{10} will bring the diagonal terms to have zero phases, without affecting $|00\rangle$ or $|11\rangle$ state. Also notice that such single-qubit rotations remove the phase term $\delta t_{\rm gate}/2$, thus the phase factor $e^{i\delta t_{\rm gate}/2}$ will

disappear in the local equivalent form. After this step, assuming that the only prominent process other than the off-resonant Rabi oscillation is the ZZ-rotation term, then the unitary evolution is equivalent to the unitary operator below when Eq. (13) is satisfied:

$$\hat{U}_{\sqrt{iSWAP}} = \begin{pmatrix} e^{-i\xi/2} & 0 & 0 & 0 \\ 0 & \frac{1}{\sqrt{2}} & i\frac{1}{\sqrt{2}}e^{i\gamma} & 0 \\ 0 & i\frac{1}{\sqrt{2}}e^{-i\gamma} & \frac{1}{\sqrt{2}} & 0 \\ 0 & 0 & 0 & e^{-i\xi/2} \end{pmatrix},$$
(C3)

where

$$\gamma = \arg \left[\cos \left(\frac{\Omega t_{\text{gate}}}{2} \right) - i \frac{\delta}{\Omega} \sin \left(\frac{\Omega t_{\text{gate}}}{2} \right) \right].$$
 (C4)

The operator $\hat{U}_{\sqrt{i \text{SWAP}}}$ can be locally transformed into $\hat{U}_{\text{ideal}}(\theta, \zeta)$ by virtual Z rotation before and after the Rabi oscillation

$$\hat{U}(\frac{\pi}{2},\zeta) = e^{i(\hat{Z}_1 - \hat{Z}_2)\gamma/4} \hat{U}_{\sqrt{iSWAP}} e^{-i(\hat{Z}_1 - \hat{Z}_2)\gamma/4}, \quad (C5)$$

so the phase factor γ also disappears in the final result.

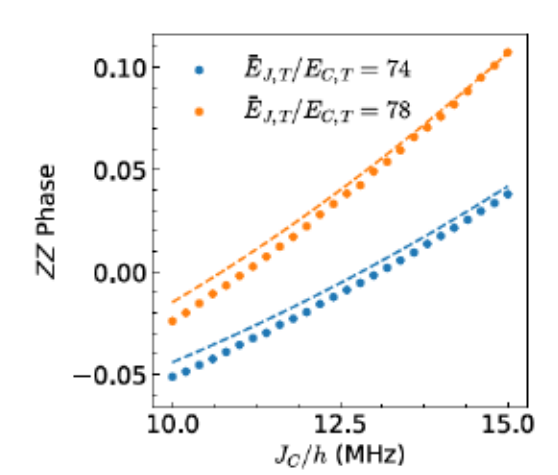


FIG. 8. Comparison between the theoretical estimation and the numerical simulation as presented in Fig. 4(b). The dots are the numerical value, and the dashed lines are the theoretical estimation.

APPENDIX D: BRANCHES AND EXTREMA OF RABI OSCILLATION FOR ONE-TONE √iswap GATE

The effectiveness of ZZ phase correction is determined by the off-resonant condition (13), and this condition has two types of extrema corresponding to the two parameters under optimization. These extrema correspond to the point in Fig. 9(e) where the plateau of zero ZZ phase turns into a line of positive slope. The first type of extrema happens at $\delta = 0$, as shown in Figs. 9(b) and 9(d), where we plot the probability of measuring the |01) and |10) state over the duration of the pulses, with the initial state to be [10]. The Rabi oscillations for both cases are close to resonance, with the difference being that panel (b) corresponds to a $3\pi/2$ rotation, while panel (d) corresponds to a $5\pi/2$ rotation. This suggests that when we make a discontinuous change in the pulse parameters during the optimization for \sqrt{iSWAP} gate around $J_C = 20$ MHz, we are actually switching to the branch of Rabi oscillation with a different

The second type of extrema is related to the parameter g_{eff} , as shown in Fig. 10. While specific values of $g_{01,10}$ might help correct the ZZ phase error, the maximum swapping probability for this particular $g_{01,10}$ can be less than 1/2, making the swapping insufficient. The optimization then will prioritize condition (13), leaving ZZ phase error to be only partially corrected. This case is shown in

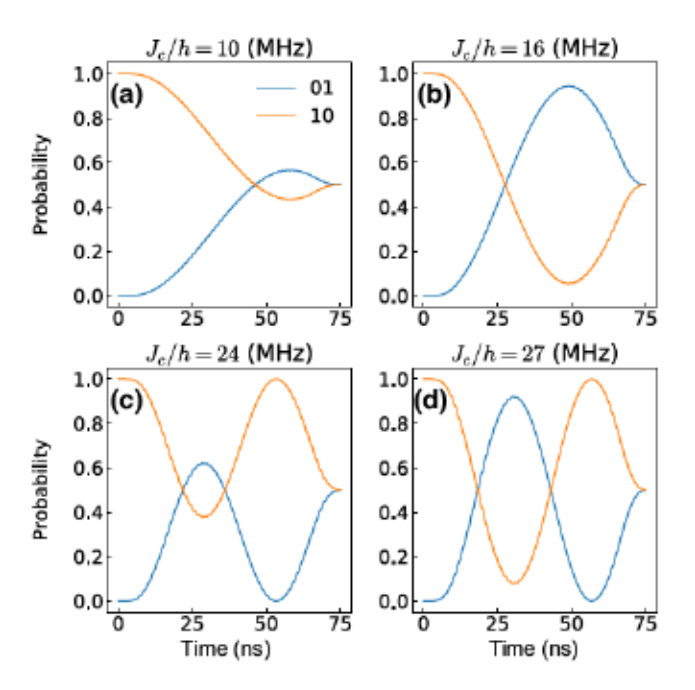


FIG. 9. The probability evolution with initial state $|10\rangle$ for (a) $J_c = 10$ MHz, (b) 16 MHz, (c) 24 MHz, (d) 27 MHz. The vertical axis is the probability of measuring state $|01\rangle$ or $|10\rangle$. The result is obtained using the optimized pulse parameters of the corresponding points in Fig. 6.

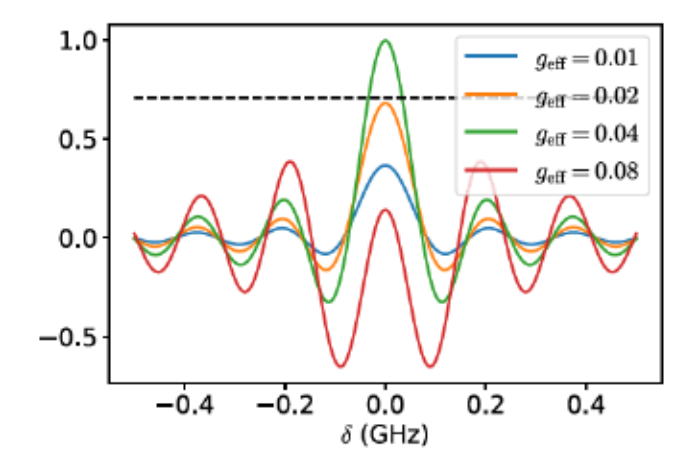


FIG. 10. Evaluation of the term on the left-hand side of the condition (13) for different $g_{01,10}$. The black dashed line indicates where the curves cross $1/\sqrt{2}$ (the $-1/\sqrt{2}$ line is out of the range of the plot). For the detuning range $|\delta| \le 0.5$ GHz, the curve does not necessarily reach the value $\pm 1/\sqrt{2} \approx 0.707$.

panel (c) of Fig. 9 where the amplitude of the probability oscillation is close to 1/2.

- G. S. Paraoanu, Microwave-induced coupling of superconducting qubits, Phys Rev. B 74, 140504 (2006).
- [2] J. M. Chow, J. M. Gambetta, A. W. Cross, S. T. Merkel, C. Rigetti, and M. Steffen, Microwave-activated conditionalphase gate for superconducting qubits, New J. Phys. 15, 115012 (2013).
- [3] S. Krinner, P. Kurpiers, B. Royer, P. Magnard, I. Tsitsilin, J.-C. Besse, A. Remm, A. Blais, and A. Wallraff, Demonstration of an all-microwave controlled-phase gate between far-detuned qubits, Phys. Rev. Appl. 14, 044039 (2020).
- [4] B. K. Mitchell, R. K. Naik, A. Morvan, A. Hashim, J. M. Kreikebaum, B. Marinelli, W. Lavrijsen, K. Nowrouzi, D. I. Santiago, and I. Siddiqi, Hardware-efficient microwave-activated tunable coupling between superconducting qubits, Phys. Rev. Lett. 127, 200502 (2021).
- [5] J. M. Chow, A. D. Córcoles, J. M. Gambetta, C. Rigetti, B. R. Johnson, J. A. Smolin, J. R. Rozen, G. A. Keefe, M. B. Rothwell, M. B. Ketchen, and M. Steffen, Simple all-microwave entangling gate for fixed-frequency superconducting qubits, Phys. Rev. Lett. 107, 080502 (2011).
- [6] S. Sheldon, E. Magesan, J. M. Chow, and J. M. Gambetta, Procedure for systematically tuning up cross-talk in the cross-resonance gate, Phys. Rev. A 93, 060302 (2016).
- [7] A. Kandala, K. X. Wei, S. Srinivasan, E. Magesan, S. Carnevale, G. A. Keefe, D. Klaus, O. Dial, and D. C. McKay, Demonstration of a high-fidelity CNOT Gate for fixed-frequency transmons with engineered ZZ suppression, Phys. Rev. Lett. 127, 130501 (2021).
- [8] J. Koch, T. M. Yu, J. Gambetta, A. A. Houck, D. I. Schuster, J. Majer, A. Blais, M. H. Devoret, S. M. Girvin, and R. J. Schoelkopf, Charge-insensitive qubit design derived from the Cooper pair box, Phys. Rev. A 76, 042319 (2007).

- [9] A. Morvan, L. Chen, J. M. Larson, D. I. Santiago, and I. Siddiqi, Optimizing frequency allocation for fixedfrequency superconducting quantum processors, Phys. Rev. Res. 4, 023079 (2022).
- [10] L. DiCarlo, J. M. Chow, J. M. Gambetta, L. S. Bishop, B. R. Johnson, D. I. Schuster, J. Majer, A. Blais, L. Frunzio, S. M. Girvin, and R. J. Schoelkopf, Demonstration of two-qubit algorithms with a superconducting quantum processor, Nature 460, 240 (2009).
- [11] T. Yamamoto, M. Neeley, E. Lucero, R. C. Bialczak, J. Kelly, M. Lenander, M. Mariantoni, A. D. O'Connell, D. Sank, H. Wang, M. Weides, J. Wenner, Y. Yin, A. N. Cleland, and J. M. Martinis, Quantum process tomography of two-qubit controlled-Z and controlled-not gates using superconducting phase qubits, Phys. Rev. B 82, 184515 (2010).
- [12] Y. Chen, et al., Qubit architecture with high coherence and fast tunable coupling, Phys. Rev. Lett. 113, 220502 (2014).
- [13] D. C. McKay, R. Naik, P. Reinhold, L. S. Bishop, and D. I. Schuster, High-contrast qubit interactions using multimode cavity QED, Phys. Rev. Lett. 114, 080501 (2015).
- [14] R. Barends, et al., Diabatic gates for frequency-tunable superconducting qubits, Phys. Rev. Lett. 123, 210501 (2019).
- [15] R. Schutjens, F. A. Dagga, D. J. Egger, and F. K. Wilhelm, Single-qubit gates in frequency-crowded transmon systems, Phys. Rev. A 88, 052330 (2013).
- [16] F. Beaudoin, M. P. da Silva, Z. Dutton, and A. Blais, First-order sidebands in circuit QED using qubit frequency modulation, Phys. Rev. A 86, 022305 (2012).
- [17] J. D. Strand, M. Ware, F. Beaudoin, T. A. Ohki, B. R. Johnson, A. Blais, and B. L. T. Plourde, First-order sideband transitions with flux-driven asymmetric transmon qubits, Phys. Rev. B 87, 220505 (2013).
- [18] R. K. Naik, N. Leung, S. Chakram, P. Groszkowski, Y. Lu, N. Earnest, D. C. McKay, J. Koch, and D. I. Schuster, Random access quantum information processors using multimode circuit quantum electrodynamics, Nat. Commun. 8, 1904 (2017).
- [19] N. Didier, E. A. Sete, M. P. da Silva, and C. Rigetti, Analytical modeling of parametrically modulated transmon qubits, Phys. Rev. A 97, 022330 (2018).
- [20] S. A. Caldwell, et al., Parametrically activated entangling gates using transmon qubits, Phys. Rev. Appl. 10, 034050 (2018).
- [21] M. Reagor, et al., Demonstration of universal parametric entangling gates on a multi-qubit lattice, Sci. Adv. 4, eaao3603 (2018).
- [22] S. S. Hong, A. T. Papageorge, P. Sivarajah, G. Crossman, N. Didier, A. M. Polloreno, E. A. Sete, S. W. Turkowski, M. P. da Silva, and B. R. Johnson, Demonstration of a parametrically activated entangling gate protected from flux noise, Phys. Rev. A 101, 012302 (2020).
- [23] E. A. Sete, N. Didier, A. Q. Chen, S. Kulshreshtha, R. Manenti, and S. Poletto, Parametric-resonance entangling gates with a tunable coupler, Phys. Rev. Appl. 16, 024050 (2021).
- [24] P. Bertet, C. J. P. M. Harmans, and J. E. Mooij, Parametric coupling for superconducting qubits, Phys. Rev. B 73, 064512 (2006).

- [25] A. O. Niskanen, Y. Nakamura, and J.-S. Tsai, Tunable coupling scheme for flux qubits at the optimal point, Phys. Rev. B 73, 094506 (2006).
- [26] A. O. Niskanen, K. Harrabi, F. Yoshihara, Y. Nakamura, S. Lloyd, and J. S. Tsai, Quantum coherent tunable coupling of superconducting qubits, Science 316, 723 (2007).
- [27] D. C. McKay, S. Filipp, A. Mezzacapo, E. Magesan, J. M. Chow, and J. M. Gambetta, Universal gate for fixed-frequency qubits via a tunable bus, Phys. Rev. Appl. 6, 064007 (2016).
- [28] B. Royer, A. L. Grimsmo, N. Didier, and A. Blais, Fast and high-fidelity entangling gate through parametrically modulated longitudinal coupling, Quantum 1, 11 (2017).
- [29] M. Ganzhorn, G. Salis, D. J. Egger, A. Fuhrer, M. Mergenthaler, C. Müller, P. Müller, S. Paredes, M. Pechal, M. Werninghaus, and S. Filipp, Benchmarking the noise sensitivity of different parametric two-qubit gates in a single superconducting quantum computing platform, Phys. Rev. Res. 2, 033447 (2020).
- [30] J. A. Valery, S. Chowdhury, G. Jones, and N. Didier, Dynamical sweet spot engineering via two-tone flux modulation of superconducting qubits, PRX Quantum 3, 020337 (2022).
- [31] M. D. Hutchings, J. B. Hertzberg, Y. Liu, N. T. Bronn, G. A. Keefe, M. Brink, J. M. Chow, and B. L. T. Plourde, Tunable superconducting qubits with flux-independent coherence, Phys. Rev. Appl. 8, 044003 (2017).
- [32] T. W. Larsen, K. D. Petersson, F. Kuemmeth, T. S. Jespersen, P. Krogstrup, J. Nygård, and C. M. Marcus, Semiconductor-nanowire-based superconducting qubit, Phys. Rev. Lett. 115, 127001 (2015).
- [33] G. de Lange, B. van Heck, A. Bruno, D. J. van Woerkom, A. Geresdi, S. R. Plissard, E. P. A. M. Bakkers, A. R. Akhmerov, and L. DiCarlo, Realization of microwave quantum circuits using hybrid superconductingsemiconducting nanowire Josephson elements, Phys. Rev. Lett. 115, 127002 (2015).
- [34] L. Casparis, M. R. Connolly, M. Kjaergaard, N. J. Pearson, A. Kringhøj, T. W. Larsen, F. Kuemmeth, T. Wang, C. Thomas, S. Gronin, G. C. Gardner, M. J. Manfra, C. M. Marcus, and K. D. Petersson, Superconducting gatemon qubit based on a proximitized two-dimensional electron gas, Nat. Nanotechnol. 13, 915 (2018).
- [35] A. Hertel, M. Eichinger, L. O. Andersen, D. M. van Zanten, S. Kallatt, P. Scarlino, A. Kringhøj, J. M. Chavez-Garcia, G. C. Gardner, S. Gronin, M. J. Manfra, A. Gyenis, M. Kjaergaard, C. M. Marcus, and K. D. Petersson, Gate-tunable transmon using selective-area-grown superconductor-semiconductor hybrid structures on silicon, Phys. Rev. Appl. 18, 034042 (2022).
- [36] A. Kringhøj, B. van Heck, T. W. Larsen, O. Erlandsson, D. Sabonis, P. Krogstrup, L. Casparis, K. D. Petersson, and C. M. Marcus, Suppressed charge dispersion via resonant tunneling in a single-channel transmon, Phys. Rev. Lett. 124, 246803 (2020).
- [37] N. Sundaresan, I. Lauer, E. Pritchett, E. Magesan, P. Jurcevic, and J. M. Gambetta, Reducing unitary and spectator errors in cross resonance with optimized rotary echoes, PRX Quantum 1, 020318 (2020).
- [38] P. Mundada, G. Zhang, T. Hazard, and A. Houck, Suppression of qubit crosstalk in a tunable coupling superconducting circuit, Phys. Rev. Appl. 12, 054023 (2019).

- [39] M. C. Collodo, J. Herrmann, N. Lacroix, C. K. Andersen, A. Remm, S. Lazar, J.-C. Besse, T. Walter, A. Wallraff, and C. Eichler, Implementation of conditional phase gates based on tunable ZZ interactions, Phys. Rev. Lett. 125, 240502 (2020).
- [40] R. Aguado, A perspective on semiconductor-based superconducting qubits, Appl. Phys. Lett. 117, 240501 (2020).
- [41] It is also common to write the Jaynes-Cummings coupling constant g = 4J_C(E_{JF}E_{J,T}/4E_{C,F}E_{C,T})^{1/4}.
- [42] J. Zhang, J. Vala, S. Sastry, and K. B. Whaley, Geometric theory of nonlocal two-qubit operations, Phys. Rev. A 67, 042313 (2003).
- [43] K. N. Nesterov, Q. Ficheux, V. E. Manucharyan, and M. G. Vavilov, Proposal for entangling gates on fluxonium qubits via a two-photon transition, PRX Quantum 2, 020345 (2021).
- [44] D. C. McKay, C. J. Wood, S. Sheldon, J. M. Chow, and J. M. Gambetta, Efficient Z gates for quantum computing, Phys. Rev. A 96, 022330 (2017).
- [45] L. H. Pedersen, N. M. Møller, and K. Mølmer, Fidelity of quantum operations, Phys. Lett. A 367, 47 (2007).
- [46] S. Krinner, N. Lacroix, A. Remm, A. D. Paolo, E. Genois, C. Leroux, C. Hellings, S. Lazar, F. Swiadek, J. Herrmann, G. J. Norris, C. K. Andersen, M. Müller, A. Blais, C. Eichler, and A. Wallraff, Realizing repeated quantum error correction in a distance-three surface code, Nature 605, 669 (2022).
- [47] N. Schuch and J. Siewert, Natural two-qubit gate for quantum computation using the XY interaction, Phys. Rev. A 67, 032301 (2003).
- [48] P. J. J. O'Malley, et al., Qubit metrology of ultralow phase noise using randomized benchmarking, Phys. Rev. Appl. 3, 044009 (2015).
- [49] V. Tripathi, M. Khezri, and A. N. Korotkov, Operation and intrinsic error budget of a two-qubit cross-resonance gate, Phys. Rev. A 100, 012301 (2019).
- [50] M. A. Nielsen, A simple formula for the average gate fidelity of a quantum dynamical operation, Phys. Lett. A 303, 249 (2002).

- [51] A. G. Fowler, M. Mariantoni, J. M. Martinis, and A. N. Cleland, Surface codes: Towards practical large-scale quantum computation, Phys. Rev. A 86, 032324 (2012).
- [52] B. M. Varbanov, F. Battistel, B. M. Tarasinski, V. P. Ostroukh, T. E. O'Brien, L. DiCarlo, and B. M. Terhal, Leakage detection for a transmon-based surface code, npj Quantum Inf. 6, 102 (2020).
- [53] C. Huang, X. Ni, F. Zhang, M. Newman, D. Ding, X. Gao, T. Wang, H.-H. Zhao, F. Wu, G. Zhang, C. Deng, H.-S. Ku, J. Chen, and Y. Shi, Alibaba cloud quantum development platform: Surface code simulations with crosstalk, arXiv:2002.08918 [quant-ph] (2020).
- [54] F. Luthi, T. Stavenga, O. W. Enzing, A. Bruno, C. Dickel, N. K. Langford, M. A. Rol, T. S. Jespersen, J. Nygård, P. Krogstrup, and L. DiCarlo, Evolution of nanowire transmon qubits and their coherence in a magnetic field, Phys. Rev. Lett. 120, 100502 (2018).
- [55] W. M. Strickland, B. H. Elfeky, J. O. Yuan, W. F. Schiela, P. Yu, D. Langone, M. G. Vavilov, V. E. Manucharyan, and J. Shabani, Superconducting resonators with voltagecontrolled frequency and nonlinearity, Phys. Rev. Appl. 19, 034021 (2023).
- [56] M. Viana and J. Espinar, Differential Equations: A Dynamical Systems Approach to Theory and Practice, Graduate Studies in Mathematics (American Mathematical Society, Providence in Rhode Island, 2021).
- [57] M. Abramowitz, Handbook of Mathematical Functions, with Formulas, Graphs, and Mathematical Tables (Dover Publications Inc., USA, 1974).
- [58] H. Paik, A. Mezzacapo, M. Sandberg, D. T. McClure, B. Abdo, A. D. Córcoles, O. Dial, D. F. Bogorin, B. L. T. Plourde, M. Steffen, A. W. Cross, J. M. Gambetta, and J. M. Chow, Experimental demonstration of a resonator-induced phase gate in a multiqubit circuit-QED system, Phys. Rev. Lett. 117, 250502 (2016).
- [59] H. Xiong, Q. Ficheux, A. Somoroff, L. B. Nguyen, E. Dogan, D. Rosenstock, C. Wang, K. N. Nesterov, M. G. Vavilov, and V. E. Manucharyan, Arbitrary controlled-phase gate on fluxonium qubits using differential ac stark shifts, Phys. Rev. Res. 4, 023040 (2022).